

Thermodynamic properties of Pt nanoparticles: Size, shape, support, and adsorbate effectsB. Roldan Cuenya,^{1,*} M. Alcántara Ortigoza,^{1,†} L. K. Ono,¹ F. Behafarid,¹ S. Mostafa,¹ J. R. Croy,¹ K. Paredis,¹ G. Shafai,¹ T. S. Rahman,¹ L. Li,² Z. Zhang,² and J. C. Yang³¹*Department of Physics, PS 430, University of Central Florida, P.O. Box 162385, 4000 Central Florida Boulevard, Orlando, Florida 32816, USA*²*Department of Mechanical Engineering and Materials Science, University of Pittsburgh, Pittsburgh, Pennsylvania 15261, USA*³*Department of Chemical and Petroleum Engineering, University of Pittsburgh, Pittsburgh, Pennsylvania 15261, USA*

(Received 16 October 2011; revised manuscript received 16 November 2011; published 20 December 2011)

This study presents a systematic investigation of the thermodynamic properties of free and γ -Al₂O₃-supported size-controlled Pt nanoparticles (NPs) and their evolution with decreasing NP size. A combination of *in situ* extended x-ray absorption fine-structure spectroscopy (EXAFS), *ex situ* transmission electron microscopy (TEM) measurements, and NP shape modeling revealed (i) a cross over from positive to negative thermal expansion with decreasing particle size, (ii) size- and shape-dependent changes in the mean square bond-projected bond-length fluctuations, and (iii) enhanced Debye temperatures (Θ_D , relative to bulk Pt) with a bimodal size-dependence for NPs in the size range of \sim 0.8–5.4 nm. For large NP sizes (diameter $d > 1.5$ nm) Θ_D was found to decrease toward Θ_D of bulk Pt with increasing NP size. For NPs ≤ 1 nm, a monotonic decrease of Θ_D was observed with decreasing NP size and increasing number of low-coordinated surface atoms. Our density functional theory calculations confirm the size- and shape-dependence of the vibrational properties of our smallest NPs and show how their behavior may be tuned by H desorption from the NPs. The experimental results can be partly attributed to thermally induced changes in the coverage of the adsorbate (H_2) used during the EXAFS measurements, bearing in mind that the interaction of the Pt NPs with the stiff, high-melting temperature γ -Al₂O₃ support may also play a role. The calculations also provide good qualitative agreement with the trends in the mean square bond-projected bond-length fluctuations measured via EXAFS. Furthermore, they revealed that part of the Θ_D enhancement observed experimentally for the smallest NPs ($d \leq 1$ nm) might be assigned to the specific sensitivity of EXAFS, which is intrinsically limited to bond-projected bond-length fluctuations.

DOI: [10.1103/PhysRevB.84.245438](https://doi.org/10.1103/PhysRevB.84.245438)

PACS number(s): 61.05.cj, 61.46.Df, 71.15.Mb, 82.60.Qr

I. INTRODUCTION

Metal nanoparticles (NPs) have been shown to display anomalous electronic and thermodynamic properties, including metal to nonmetal transitions,^{1,2} superheating,³ and negative thermal expansion.^{4–7} However, despite decades of intense research, the origin of these effects is still heavily debated. Consensus exists regarding the strong influence of the NP size on the thermal properties of nanoscale materials,⁸ but further investigations are required in order to understand specific size-dependent trends. It has been suggested that NPs within different size regimes must be treated differently. For example, nonmonotonic variations in the melting point (T_m) of small (<200 atoms) size-selected clusters have been observed^{9,10} and assigned to the interplay of electronic and geometric effects.⁹ However, the relative contribution of such effects could not be separated. For larger NPs (>200 atoms) monotonic size-dependent trends in T_m were observed.¹¹ For a given material system the specific thermal behavior was found to be drastically affected by environmental influences such as the presence of a support, an encapsulating matrix, the internal defect density within a NP, the structural and chemical nature of the NP/support interface, and the presence of ligands or surface adsorbates.^{12–17}

Reduced melting and Debye (Θ_D) temperatures with respect to bulk have been generally reported for free-standing as well as supported NP systems.^{11,18–25} In addition a correlation between T_m and the NP diameter has been commonly observed: decreased T_m with decreasing NP size.³ Since

for bulk systems T_m is proportional to Θ_D^2 (Lindemann's criterion²⁶), the Debye temperature is also expected to decrease in clusters relative to the bulk.²⁷ Nevertheless, increased Θ_D and superheating have been observed via a variety of methods [e.g., transmission electron microscopy (TEM), x-ray diffraction, differential scanning calorimetry, extended x-ray absorption fine-structure spectroscopy (EXAFS), etc.] for several nanoscale material systems, including supported or embedded Pt,^{5,6,28,29} Ag,¹⁷ and Ge NPs,^{16,30,31} as well as unsupported nanocrystalline agglomerates such as Ag,³² Au,³² ZnS,¹² and thiol-capped CdS¹³ and CdTe¹⁴ nanocrystals. A comparison between the different references is challenging due to the distinct sample preparation and characterization conditions and, in some cases, the lack of detail on the specific structure of the systems investigated. However, some interesting trends could be extracted from the literature. Enhanced thermal stability and superheating was detected for faceted NP shapes with good crystallinity and coherent or semicoherent (nearly epitaxial) interfaces around the embedded NPs, or when NPs were coated by a high melting-point matrix.^{16,33,34} On the other hand reduced T_m values were found for NPs randomly embedded (e.g., without epitaxial relationships) in similar matrixes. According to previous studies, internal defects within the NPs or at the NP/support interface, voids, impurities, grain boundaries, as well as low-coordinated surface atoms (for NPs not fully embedded in a support matrix) act as nucleation sites for the onset of heterogeneous melting.³ Therefore, a global understanding of the thermodynamic properties of nanoscale materials requires in-depth insight into

their geometrical structure, including its modifications in the presence of an environment (support and/or adsorbate).

In addition to the anomalous melting/vibrational behavior described previously, a number of additional material properties were found to be modified at the nanoscale. For instance, changes in the electronic properties (e.g., discretization of the energy levels) of small NPs, together with the interaction with the NP support, were held responsible for a size-dependent crossover from positive to negative thermal expansion observed with decreasing NP size for some NP systems^{5,6,20} or with increasing sample temperature for a given NP size.³⁵ However, most of the experimental data reported thus far were collected on NPs exposed to a certain environment, for example, in the presence of hydrogen,³⁶ and the role of such adsorbates on their thermodynamic properties is yet to be fully understood. It is well known that H lifts the contraction that the bonds of Pt NPs undergo because of low coordination either partially^{6,28,37,38} or almost totally.³⁹ On the other hand the effective hydrogen coverage on the NP surface might vary in the course of an experimental thermal cycle. Interestingly, while Pt(111) can be saturated with hydrogen at 85 K and nearly complete H desorption has been observed in vacuum above 400 K,⁴⁰ Pt NPs on Al₂O₃ have been reported to become free of H only above 550 K.³⁷ An in-depth investigation of the role of H desorption from NPs in the thermal expansion or contraction observed experimentally under constant H₂ flow is still lacking. The calculations presented here provide insight into the thermal stability of adsorbed H species on Pt NPs and help evaluate the changes in the bond lengths brought about by the adsorption of H and their contribution to the negative thermal expansion observed for small Pt NPs.

It is evident that the trends described previously are intimately related to the complex structure of the nano-sized materials, and a detailed atomic-scale investigation of the origin of these anomalies is yet to be undertaken. This study focuses on the investigation of the influence of the NP geometry (size and shape) and environment (adsorbate and support) on the thermal properties of structurally well-defined, free-, and γ -Al₂O₃-supported Pt NPs. For this purpose we have taken advantage of state-of-the-art nanostructure fabrication (micelle encapsulation) and characterization methods (EXAFS, TEM, and cluster-shape modeling), as well as of first-principles theoretical calculations [density functional theory (DFT)]. In particular, insight into the evolution of important material characteristics such as the thermal expansion coefficient (α) and the Debye temperature with decreasing NP size is provided. Our calculations serve to separate intrinsic (free NPs) from adsorbate (*H*)-induced changes in the Pt-Pt distances measured at different temperatures. They also revealed drastic differences between the conventional mean square atomic displacement (MSD) and the mean-square bond-length fluctuations (MSBLF) parallel to the bond obtained from the analysis of EXAFS data of NPs.

II. EXPERIMENTAL AND THEORETICAL METHODS

A. Sample preparation and morphological characterization (TEM)

Size- and shape-selected Pt NPs were prepared by micelle encapsulation methods. Commercially available

poly(styrene)-block-poly(2vinylpyridine) [PS-P2VP] diblock copolymers were dissolved in toluene to form inverse micelles. Size-selected Pt NPs are created by dissolving H₂PtCl₆ into the polymeric solution. Subsequently, the nanocrystalline γ -Al₂O₃ support (average size \sim 40 nm) is added. The encapsulating ligands are eliminated by annealing in O₂ at 648 K for 24 hours. Different NP sizes can be obtained by changing the molecular weight of the head (P2VP) of the encapsulating polymer, the metal/P2VP ratio (micelle loading), and the post preparation annealing treatment and atmosphere.³⁸ Our micellar synthesis normally leads to 3D-like NP structures. Nevertheless, the NP shape can be changed from 3D to 2D by decreasing the metal loading into the initially spherical polymeric micelles. Further details on the sample preparation method and synthesis parameters can be found in Refs. 28, 38, and 41–44, and Table I.







TEM samples were prepared by making an ethanol suspension of the Pt/ γ -Al₂O₃ powder and placing a few drops of this liquid onto an ultrathin C-coated Cu grid and allowing the sample to dry in air. High-angle annular dark-field (HAADF) images of the Pt/ γ -Al₂O₃ samples were acquired under scanning mode within a JEM 2100F TEM operated at 200 kV. The probe size of the scanning transmission electron microscopy (STEM) is about 0.2 nm. The Pt NP diameters were determined by measuring the full width at half maximum of the HAADF intensity profile across the individual Pt NPs. Average and volume-weighted TEM diameters are shown in Table I. The TEM images shown here were acquired after the EXAFS measurements. NP sintering did not take place in the course of the EXAFS measurements since the samples were previously stabilized by a 24-h annealing treatment at the maximum temperature of the EXAFS thermal cycle (648 K).

B. Structural and vibrational characterization (EXAFS) and NP shape modeling

EXAFS data were acquired at beamline X18B of the NSLS at Brookhaven National Laboratory in transmission mode using the Pt L₃ edge. The EXAFS samples were prepared by pressing the Pt/ γ -Al₂O₃ powders into thin pellets, which were mounted in a sample cell that permitted sample heating and liquid nitrogen cooling, as well as the continuous flow of gases during data acquisition. A bulk Pt foil was measured simultaneously with all samples (in reference mode) for energy alignment and calibration purposes. Multiple scans (up to 6) were collected at each temperature of interest and averaged in order to improve the signal-to-noise ratio. Measurements were done at different temperatures under H₂ (50% H₂ balanced with He for a total flow rate of 50 ml/min, samples S1–S9 in Table I) and He (S2) atmospheres.

Data processing was conducted with the IFEFFIT package⁴⁵ by simultaneously analyzing the first shell Pt-Pt contribution of the data acquired at different temperatures. The EXAFS Debye-Waller factors (σ^2) were obtained by using the Correlated Debye Model (CDM),⁴⁶ as described in Ref. 28. From the analysis of temperature-dependent EXAFS data, the dynamic mean-square relative bond-length disorder σ_d^2 was extracted, and through that Θ_D . In the high-temperature approximation $\sigma_d^2 = k_B T/k \sim T/\Theta_D^2$, with k being the effective

TABLE I. Parameters used for the synthesis of micellar Pt NPs, including polymer type (PS-PVP) and the ratio (L) between the metal-salt loading and the molecular weight of the polymer head (P2VP). Also included are the mean and the volume-weighted TEM diameters. By comparing structural information obtained via EXAFS (first–fourth NN coordination numbers) and TEM (NP diameters) with a database containing fcc-cluster shapes, the ratio of the number of surface atoms to the total number of atoms in a NP (N_s/N_t) and the ratio of the number of atoms in contact with the substrate to the total number of atoms (N_c/N_t) were obtained. The static disorders (σ_s^2) obtained from the analysis of EXAFS data are also shown. The largest values of σ_s^2 were generally observed for the samples with the largest NP/support interface (S1 and S4).

Sample name	Polymer	L	TEM diameter (nm)	Volume-weighted TEM diameter (nm)	σ_s^2 (\AA^2)	Model cluster shapes	N_t	N_s/N_t	N_c/N_t
S1	PS(27700)–P2VP(4300)	0.06	0.8 (0.2)	0.9 (0.3)	0.0023(2)		22	0.86	0.55
S2	PS(27700)–P2VP(4300)	0.1	0.8 (0.2)	0.9 (0.2)	0.0013(2)		44	0.84	0.23
S3	PS(27700)–P2VP(4300)	0.2	1.0 (0.2)	1.2 (0.2)	0.0010(3)		85	0.74	0.18
S4	PS(16000)–P2VP(3500)	0.05	1.0 (0.2)	1.1 (0.2)	0.0028(3)		33	0.82	0.55
S5	PS(16000)–P2VP(3500)	0.1	1.0 (0.2)	1.2 (0.3)	0.0019(2)		55	0.75	0.16
S6	PS(16000)–P2VP(3500)	0.2	1.0 (0.2)	1.1 (0.3)	0.0015(2)		140	0.64	0.13
S7	PS(16000)–P2VP(3500)	0.4	1.8 (1.5)	5.7 (2.2)	0.0015(2)				
S8	PS(27700)–P2VP(4300)	0.3	3.3 (1.5)	6.0 (2.8)	0.0016(1)				
S9	PS(27700)–P2VP(4300)	0.6	5.4 (3.0)	15.0 (10.0)	0.0012(1)				

force constant.^{47,48} Hence, the slope of the temperature dependence of σ_d^2 is inversely proportional to Θ_D^2 . The static disorders ($\sigma_s^2 = \sigma^2 - \sigma_d^2$) are shown in Table I. The latter parameter is considered a measure of the degree of anisotropy in the internal structure of NPs (distribution in bond lengths), which for small clusters can be intrinsic⁴⁹ but are also strongly influenced by the underlying support.⁵⁰

Quantitative determination of the NP shape was carried out by analyzing low temperature EXAFS data up to the fourth nearest-neighbor (NN) contribution, including multiple scattering (MS), as described in Refs. 38, 43, and references therein. The data were acquired in H_2 after NP reduction. References 28, 38, and 43 contain analogous information for the rest of the samples discussed in the present article. The shapes of our Pt NPs have been resolved by matching structural information obtained experimentally via EXAFS (coordination numbers up to the fourth NN, N_1 – N_4) and TEM (NP diameter, d) to analogous data extracted from a database containing ~ 4000 model fcc NP shapes. In our analysis, after taking into consideration the error bars in the EXAFS coordination numbers as well as the TEM diameters, we have found on average three model fcc cluster shapes consistent with all experimental parameters (N_1 , N_2 , N_3 , N_4 , and d) for the small NPs. A larger degeneracy of NP shapes in agreement

with the previous experimental parameters was found for the large NPs (>1.5 nm, S7–S9), and, therefore, representative model cluster shapes for those samples are not shown here. Further details on the selection of the model NP shapes can be found in Refs. 28 and 43. A comparison of the EXAFS and model coordination numbers for the two NP shapes that best represented S1 is shown in supplementary material Table III.⁵¹ In order to determine the most representative NP shape, we have used volume-weighted TEM diameters. In general the use of the volume-weighted diameters is preferred when comparing TEM and EXAFS structural information, since EXAFS is a volume-weighted technique. Examples of the NP shapes typical of similarly prepared but larger micellar Pt NPs resolved by STM can be found in Refs. 38, 43, and 52. Table I also contains information on the total number of atoms within each NP (N_t), the ratio of the number of Pt atoms at the NP surface and perimeter to the total number of atoms (N_s/N_t), and the ratio of the number of Pt atoms in contact with the support to the total number of atoms within a NP (N_c/N_t) extracted from the selected model NP shapes. The distinction between 2D- and 3D-like NPs obtained from the former analysis is in agreement with the general trends observed here for the EXAFS static disorders, with the highest values corresponding to the 2D NPs (S1 and S4, 0.0023 and 0.0028 \AA^2 , respectively),

i.e., those with the highest relative number of atoms in contact with the support.

Changes in the morphology of our samples as a function of temperature have not been accounted for in our study, since the analysis of the thermal properties of our NPs was conducted up to a maximum annealing temperature of 648 K (for about 1.5 hours), which is the same temperature used for the 24-h sample calcination and stabilization treatment carried out prior to the EXAFS measurements. If any changes in the NP morphology (size and/or shape) were to occur at 648 K, they should have already taken place before the EXAFS measurements.

C. Computational details

Within the framework of DFT⁵³ implemented in the Vienna *ab initio* simulation package (VASP),⁵⁴ total-energy periodic super-cell calculations were performed to relax the structure and obtain the vibrational modes of clean and H-covered platinum NPs of various sizes: Pt₂₂, Pt₃₃, Pt₄₄, Pt₅₅, and Pt₈₅; Pt₂₂H₂₂, Pt₂₂H₂₅, Pt₂₂H₂₇, Pt₂₂H₂₉, and Pt₂₂H₃₁. The model NP shapes and sizes were inferred from Ref. 28 and the analysis of EXAFS and TEM data described previously. We have used pseudopotentials obtained via the projected-augmented-wave-method⁵⁵ included in VASP and applied the generalized gradient approximation for the electron-exchange correlation via the Perdew-Burke-Ernzerhof functional.⁵⁶ The Kohn-Sham orbitals are expanded in-plane waves with an energy cut off of 400.0 eV.

The intrinsic thermal expansion of a Pt₂₂ NP (model shape of S1) was obtained by using *ab initio* molecular dynamics (MD) calculations also implemented in VASP. The simulations were carried out in a canonical ensemble using a Nosé-Hoover thermostat. The relaxed structure of the Pt₂₂ NP (0 K) was thermalized at 100, 300, 500, and 700 K for 3 ps using a time step of 3 fs. In order to determine the thermal expansion, the thermal evolution of each first NN bond was traced, and an average over the entire NP obtained. Since the atoms within NPs are characterized by a wide distribution of bond lengths,⁵⁷ we report the median of the calculated first NN bond-length distribution, R .

In order to gauge the expansion induced in the Pt NPs by H desorption as a function of temperature, the evolution of the bond lengths of Pt₂₂ with varying H coverage was monitored. In principle the energetics and vibrational properties of the many possible structures that result from varying not only the H coverage but also the position and tilt angle of the H atoms should be explored. However, such an exhaustive study is computationally prohibitive. In this work we have investigated the main trends in the adsorption of hydrogen on small Pt NPs. To find the preferred sites for hydrogen adsorption, the binding energy of one H atom at the top, fcc, hcp, and bridge positions around atoms at Pt-facets and Pt-edges were obtained. Based on this information, the Pt₂₂ NP was saturated with H atoms (Pt₂₂H _{M}) at the most preferred sites (top and bridge), with $M = 22$ at facets and edges or only at edges, 25 only at edges, 27 or 29 mostly at edges, and 31 at facets and edges. In addition, it was ensured that after relaxation the nominal preferential site for H adsorption (top and bridge) remained the same. For selected H coverages, the gain in the Gibbs

free energy (G^{GAIN}) per NP upon H adsorption was calculated according to

$$G^{\text{GAIN}} = E^{\text{DFT}}(\text{Pt}_N\text{H}_M) + F_{\text{vib}}(\text{Pt}_N\text{H}_M) - E^{\text{DFT}}(\text{Pt}_N) - F_{\text{vib}}(\text{Pt}_N) - \frac{M}{2}E^{\text{DFT}}(\text{H}_2) - \frac{M}{2}\mu_{\text{H}_2}(T, P). \quad (1)$$

E^{DFT} denotes the DFT total energy (static energy at 0 K), F_{vib} denotes the vibrational Helmholtz free energy, N is the number of Pt atoms constituting the NP ($N = 22$), M is the number of H atoms on the NP, μ_{H_2} is the vibrational and kinetic part of the H₂ chemical potential taken from experiments,⁵⁸ T is the temperature, and P is the H₂ pressure, which is considered to be 1 atm. The preference of H adsorption on edge atoms of Pt₂₂ was tested through the Gibbs free energy for Pt₂₂H₂₂ by considering that (i) all H atoms adsorb at the edges and (ii) some atoms may be at facets.

The atomic MSD $\langle x^2 \rangle_{\text{th}}$ and the bond-projected MSBLF $(\sigma_d^2)_{\text{th}}$ were calculated within the harmonic approximation from the eigenfrequencies and eigenvectors. The selectivity of EXAFS for bond-length fluctuations parallel to the bond is taken into account in $(\sigma_d^2)_{\text{th}}$ by following the general theory of the EXAFS Debye-Waller factor developed by Beni and Platzman.⁵⁹ The details on the calculation of $(\sigma_d^2)_{\text{th}}$ are described elsewhere.⁵⁷

As previously mentioned, Θ^{slope} is a parameter defined in correspondence with the Debye temperature of bulk Pt and can be obtained as follows

$$\Theta^{\text{slope}} = \Theta_D^{\text{bulk Pt}} \sqrt{\frac{\Delta^{\text{bulk Pt}}}{\Delta^{\text{NP}}}}, \quad (2)$$

where $\Theta_D^{\text{bulk Pt}}$ is the Debye temperature of bulk Pt (244 K), $\Delta^{\text{bulk Pt}}$ is the slope of σ_d^2 for bulk Pt derived from EXAFS measurements ($1.528 \times 10^{-5} \text{ \AA}^2/\text{K}$)⁶, and Δ^{NP} is the slope of $(\sigma_d^2)_{\text{th}}$ calculated for the NP.

III. RESULTS

A. Morphological characterization (TEM)

The average NP-size distribution in the polymer-free micellar Pt NPs supported on $\gamma\text{-Al}_2\text{O}_3$ was obtained from HAADF-STEM images. Figure 1(a) shows a representative STEM image of Pt NPs in S1. The corresponding NP diameter histogram is displayed in Fig. 1(b), and average values for the rest of the samples are given in Table I. Additional TEM images of other samples included in this study are shown in supplementary material Fig. 1⁵¹ and Refs. 38 and 43. All of our samples containing small NPs are characterized by narrow-size distributions according to in-depth TEM analysis, while wider-size distributions were observed for some of the larger clusters. Histograms of the TEM NP diameters for all samples are given in supplementary material Fig. 2.⁵¹

B. Structural and thermodynamic properties (EXAFS)

EXAFS spectra in r -space from micellar Pt NPs supported on $\gamma\text{-Al}_2\text{O}_3$ (S1, S2, S8) are shown in Fig. 2(a). The spectra were acquired in H₂ at room temperature. The thermal evolution of the r -space EXAFS spectra of S1 measured in H₂ at temperatures ranging from 173 K to 648 K is shown

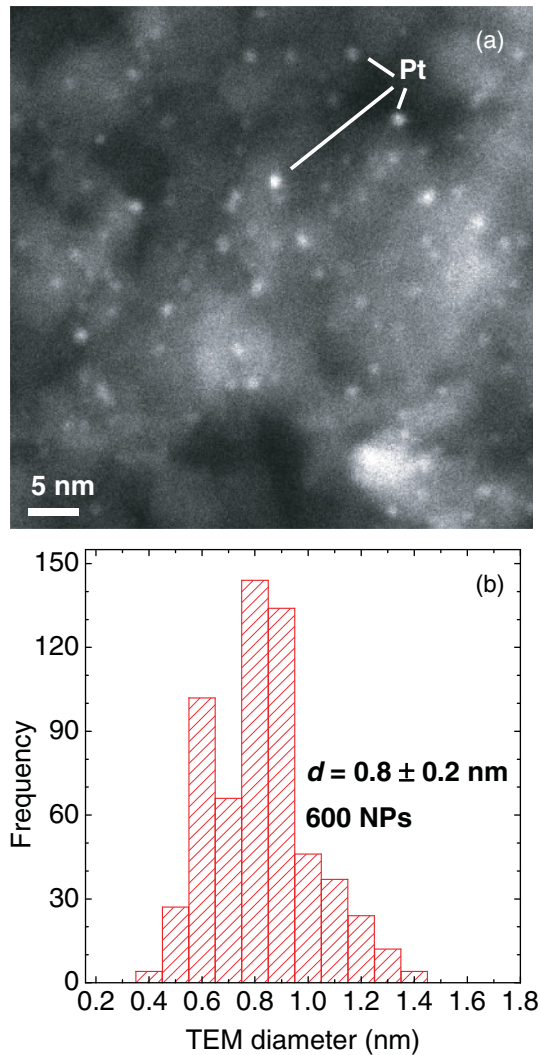


FIG. 1. (Color online) (a) HAADF-STEM image of micellar Pt NPs on γ -Al₂O₃ (S1). (b) Histogram of the NP diameter distribution.

in Fig. 2(b). With increasing temperature, a decrease in the intensity of the EXAFS signals is observed, indicative of an increase in the Pt-Pt bond-length disorder. A representative MS fit of the 173 K spectrum is included as an inset in Fig. 2(b). Supplementary material Fig. 3⁵¹ shows exemplary EXAFS data from additional samples (S1, S8, and S9) at all temperatures in k -space. Representative fits in r -space to temperature-dependent data from S1 and S8 are shown in supplementary material Figs. 4 and 5, respectively.⁵¹

Figure 3(a) displays Pt-Pt distances (R) in the temperature range of 150 K to 700 K for samples S1, S2, S7, S8, and a bulk-like Pt foil.²⁸ All measurements were carried out under continuous H₂ flow. The data points shown in Fig. 3(a) correspond to the best fit results of the experimental EXAFS spectra obtained for the first NN Pt-Pt bond lengths (R , averaged over all bonds within one NP) at different temperatures. The solid lines in Fig. 3(a) represent a linear fit of the experimental data. From the slope of such fit, the average thermal expansion coefficient (α) can be extracted: $\alpha = (1/R_0) \cdot (\partial R / \partial T)$, where R_0 is the Pt-Pt distance obtained for each sample at the lowest measurement temperature. Due to the enhanced noise of the

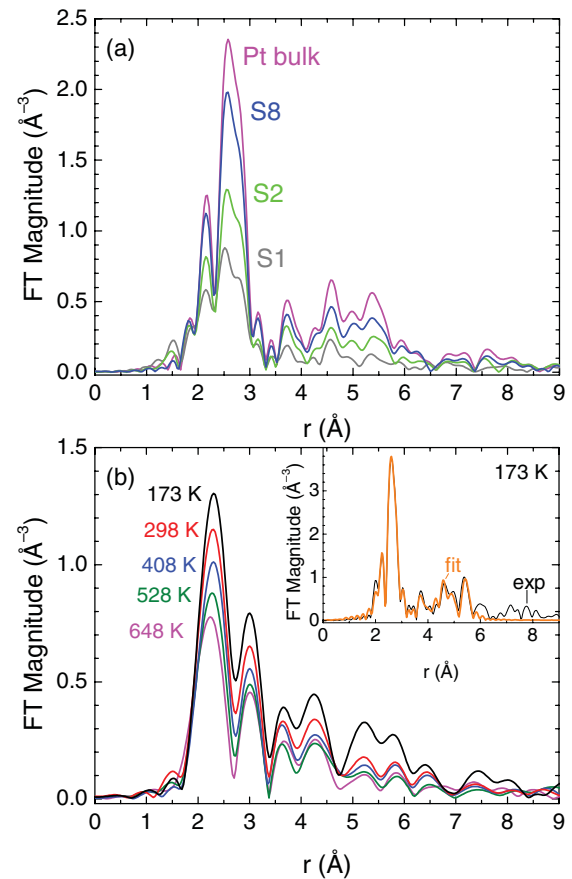


FIG. 2. (Color online) (a) k^2 -weighted EXAFS data in r -space of Pt NPs supported on γ -Al₂O₃ in samples S1, S2, S8, and a bulk Pt foil. All samples were measured in a H₂ atmosphere at room temperature after NP reduction. The range of the Fourier transform is 2–11 Å⁻¹. (b) Temperature-dependent EXAFS data in r -space of Pt NPs in S1 measured in H₂ after NP reduction. The inset displays the experimental data acquired at 173 K together with the corresponding MS fit. The ranges of the Fourier transform are 2–12 Å⁻¹ (main panel) and 2.5–17 Å⁻¹ (inset).

experimental data of sample S1 at high temperature, the Pt-Pt distance shown in Fig. 3(a) at \sim 700 K was not included in the linear fit.

Figure 4(a) depicts α (a) as a function of the average first-NN EXAFS coordination number for all samples investigated and (b) as a function of the average TEM NP diameter. In general, large coordination numbers (close to 12 for bulk Pt) are associated with large NPs and small values with small NPs, although NPs with different shapes will also display distinct coordination numbers.³⁸ Our data reveal a size-dependent trend in the thermal expansion coefficient, namely, a cross-over from positive (S3, S5–S9) to negative (S1, S2, S4) thermal expansion with decreasing NP size. The effect of hydrogen chemisorption in the thermodynamic properties of our NPs will be discussed in more detail in the theoretical section.

The dynamic correlated mean-square bond length disorder (σ_D^2) obtained from the fits of the experimental EXAFS data following the CDM⁴⁶ are shown in Fig. 5(a). As was described in the experimental section, the slope of the temperature dependence of σ_D^2 is inversely proportional to Θ_D^2 in the high

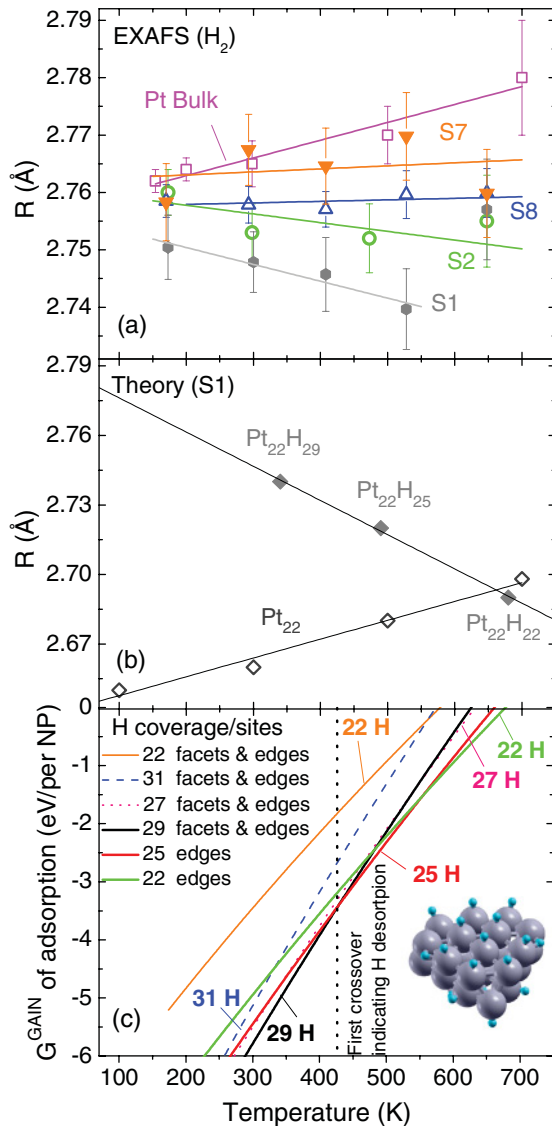


FIG. 3. (Color online) (a) Temperature-dependent Pt-Pt bond length (R) obtained from EXAFS measurements for Pt NPs supported on γ - Al_2O_3 (S1, S2, S7, S8) and a bulk Pt foil. All NP samples were measured in H_2 . (b) Calculated median of the Pt-Pt bond lengths of an unsupported clean Pt_{22} NP (open symbols, *ab initio* MD calculations) and an H-covered Pt_{22}H_M NP (solid symbols, model for S1) plotted as a function of temperature. The solid symbols in (b) correspond to H coverages that are thermodynamically stable at the given temperature (0 K DFT calculations). The median absolute deviations range from 0.04 to 0.09 Å. (c) Calculated gain in the Gibbs free energy upon H adsorption on Pt_{22} NP (model for S1) plotted as a function of temperature for varying H coverage: $\text{Pt}_{22}\text{H}_{22}$ (all H atoms on edge sites), $\text{Pt}_{22}\text{H}_{22}$ (some H atoms on facets), $\text{Pt}_{22}\text{H}_{25}$ (all H atoms on edge sites), $\text{Pt}_{22}\text{H}_{27}$, $\text{Pt}_{22}\text{H}_{29}$, and $\text{Pt}_{22}\text{H}_{31}$. The dashed line indicates the first crossover between two thermodynamically stable states (see text). The inset in (c) shows a model $\text{Pt}_{22}\text{H}_{22}$ NP with hydrogen-covering edges and facets. The small and large circles represent H and Pt atoms, respectively.

temperature approximation. Above 100 K, our experimental data display a good linear dependence at least up to our maximum measurement temperature of ~ 650 K. Deviations

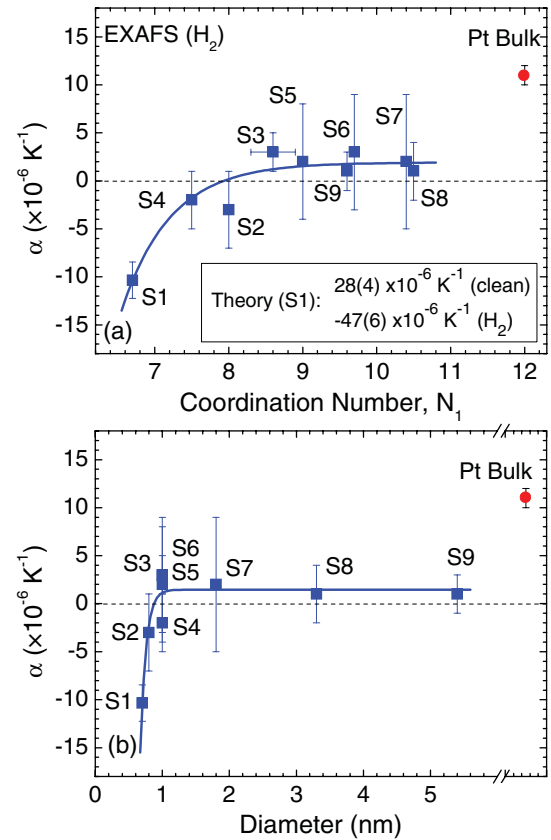


FIG. 4. (Color online) Average thermal expansion coefficient (α) extracted from the linear fit of the EXAFS data shown in Fig. 3(a) and those from additional samples described in Table II, plotted as a function of (a) the first NN coordination number, and (b) the average TEM NP diameter. The inset in (a) displays calculated thermal-expansion coefficients for an unsupported clean (adsorbate-free) Pt_{22} NP (model of S1) and an H-covered Pt_{22} NP.

from the linear behavior of σ_d^2 might be found in the proximity of the melting temperature,⁶⁰ which, even for small Pt NPs,²⁴ is expected to be significantly higher than 650 K. Our results indicate that the majority of Pt atoms in our NPs are characterized by smaller bond-projected bond-length fluctuations (correlated displacements) than those in bulk Pt samples.

The Debye temperatures obtained from the CDM analysis of our EXAFS data are displayed in Fig. 6(a) as a function of the TEM NP diameter and in Fig. 6(b) as a function of the total number of atoms in the NP normalized by the number of atoms at the NP surface and perimeter (N_t/N_s). All data correspond to samples passivated by H_2 under identical conditions. Figure 6(b) does not include data from the large NPs (S7–S9) due to the degeneracy in the model shapes obtained for those samples. A bimodal trend in Θ_D as a function of the NP diameter is observed in Fig. 6(a). For NPs ≤ 1 nm, an overall decrease of Θ_D was found with decreasing NP size [Fig. 6(a)] or decreased N_t/N_s [Fig. 6(b)]. Nevertheless, relative differences were observed for NPs with the same TEM diameter but different shape (~ 0.8 nm, S1 and S2; ~ 1 nm, S3–S6). For larger NPs (>1 nm), decreasing

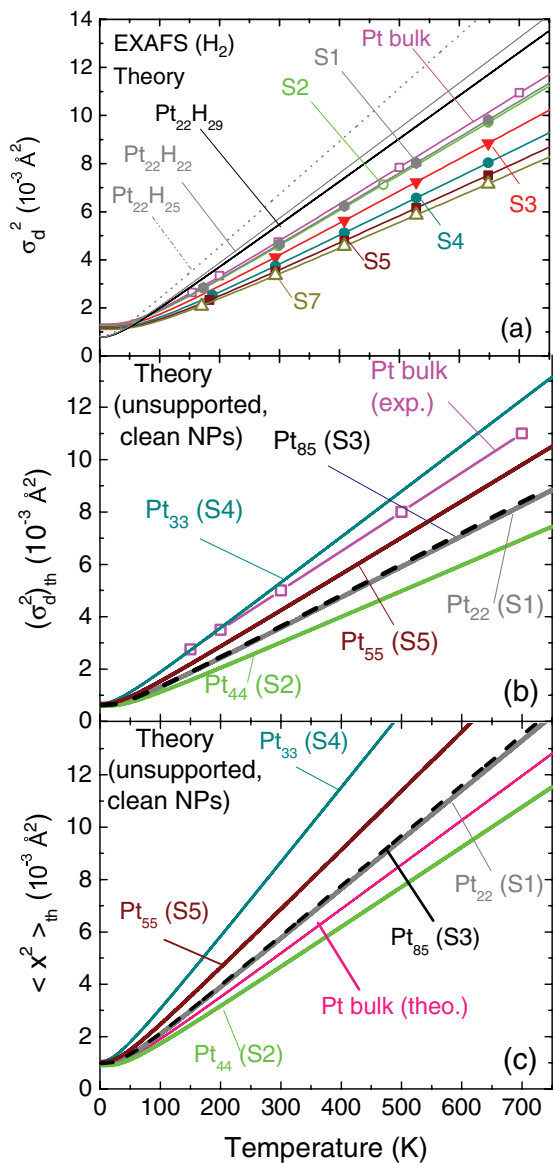


FIG. 5. (Color online) (a) Dynamic contribution (σ_d^2) to the total EXAFS Debye-Waller factor obtained for micellar Pt NPs on γ -Al₂O₃ (S1–S5, S7) under H₂ flow and analyzed with the CDM (solid lines). Symbols correspond to the temperatures at which the EXAFS data were measured. For reference, analogous data of a bulk-like Pt foil are also shown. In addition the calculated thermal evolution of the mean square bond-projected bond-length fluctuations (σ_d^2)_{th} of an H-covered Pt₂₂ NP (model of S1) for several thermodynamically stable states (Pt₂₂H₂₂, Pt₂₂H₂₅, and Pt₂₂H₂₉) are also included. (b) Thermal evolution of (σ_d^2)_{th} of unsupported, clean (H-free) model Pt NPs representative of samples S1–S5 (Pt₂₂ to Pt₈₅). (c) Mean-square displacement $\langle x^2 \rangle_{th}$ corresponding to the (σ_d^2)_{th} given in (b). For reference the EXAFS (σ_d^2) data of a Pt foil are shown in (b), and the DFT-calculated $\langle x^2 \rangle_{th}$ of bulk Pt are displayed in (c).

Debye temperatures were observed with increasing NP size (TEM diameter), approaching the bulk Θ_D value for sizes above 5 nm. Interestingly, Θ_D of all experimental NP samples was found to exceed that of bulk Pt. A detailed description of possible origins for these intriguing size- and shape-dependent trends is given in the discussion section.

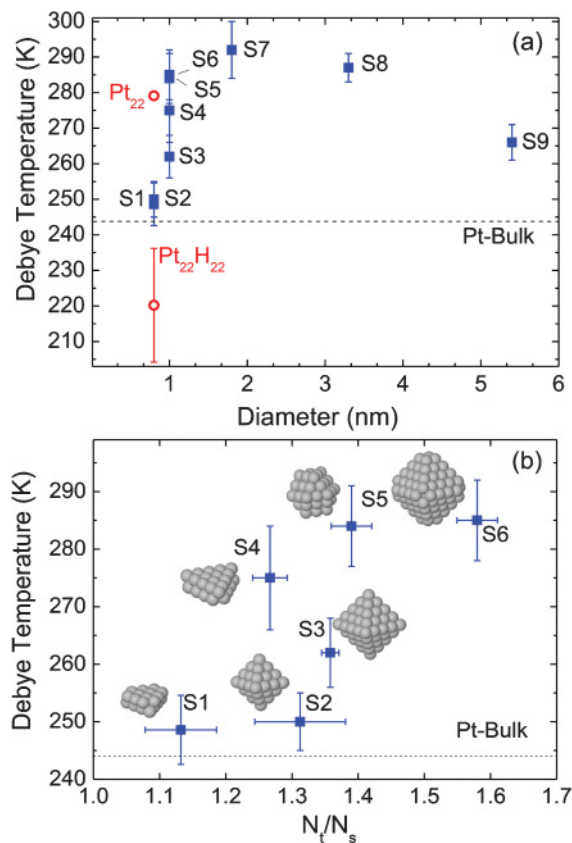


FIG. 6. (Color online) Debye temperature extracted from the CDM fit of EXAFS data displayed in Fig. 5(a) as a function of (a) the TEM NP diameter, and (b) the total number of atoms in a NP (N_t) normalized by the number of surface atoms (N_s), N_t/N_s . The values in (b) were obtained for the model NP shapes that best fitted the coordination numbers extracted from the MS analysis of low-temperature EXAFS data and the measured TEM NP diameters. The insets in (b) display the model NP shapes representative of each sample. The error margins reported for the N_t/N_s values reflect the degeneracy of NP shapes obtained as best representations of each experimental sample. The Debye temperature of a bulk-like Pt foil is also shown for reference (dashed line). In (a) the Debye temperatures calculated for Pt₂₂H₂₂ and Pt₂₂ (models for S1) are also shown.

C. Calculated structural properties and thermal expansion

DFT calculations were carried out to gain insight into the intrinsic size- and shape- dependent structural and thermodynamic properties of our NPs and the role played by the adsorbate (H₂) present during our experiments. Table II presents a comparison of the EXAFS bond lengths measured in H₂ for Pt NPs supported on γ -Al₂O₃ and the DFT-calculated median bond lengths for unsupported adsorbate-free Pt NPs (S1–S5). All values shown in Table II were normalized by the respective (experimental or calculated) bulk Pt-Pt distances at the given temperatures. Clean and unsupported model NPs show an overall contraction of 3.4–5.9% with respect to the bulk-bond lengths. Since the experiments were conducted in H₂, calculations of the effect of H chemisorption on the Pt-Pt bond lengths of one of the samples (Pt₂₂, S1) were also carried out and included in Table II. It was observed that H prefers to adsorb at top-like positions or at bridge sites (between two atoms), and binding at edge atoms is preferred, as compared

TABLE II. Experimental (EXAFS) and theoretical (DFT) average first-NN bond lengths of Pt NPs with different sizes and shapes given as a fraction of the respective bulk values. All experimental samples but S2 were H₂-passivated and supported on γ -Al₂O₃. S2 was also measured in He. The NPs analyzed theoretically were unsupported and free of adsorbates, with the exception of S1, which was also investigated with different H coverages. The experimental bulk Pt-Pt reference distances are 2.762 (2) Å at 154 K, 2.765 (4) Å at 300 K, and 2.78 (1) Å at 700 K. The calculated bulk Pt-Pt distance is 2.805 Å at 0 K. The DFT calculations were only carried out on Pt NPs containing less than 100 atoms.

Sample name	Pt-Pt bond lengths relative to bulk (EXAFS)			Pt-Pt bond lengths relative to bulk (DFT)
	172–188 K	300 K	648 K	0 K
S1	0.996	0.994	0.992	0.943 (Pt ₂₂) 0.960 (Pt ₂₂ H ₂₂) 0.969 (Pt ₂₂ H ₂₅) 0.979 (Pt ₂₂ H ₂₉) 0.964 (Pt ₄₄)
S2	0.999 (H ₂) 0.996 (He) ²⁸	0.996 (H ₂) 0.991 (He)	0.991 (H ₂) 0.982 (He)	0.975 (Pt ₈₅) 0.943 (Pt ₃₃) 0.968 (Pt ₅₅)
S3		0.999	0.995	0.975 (Pt ₈₅)
S4	0.994	0.991	0.986	0.943 (Pt ₃₃)
S5	0.996	0.993	0.990	0.968 (Pt ₅₅)
S6	0.997	0.997	0.992	
S7	0.999	1.001	0.993	
S8	0.999	0.997	0.993	
S9	0.998	0.997	0.993	

to facets. This trend is further corroborated by the Gibbs phase diagram shown in Fig. 3(c). Our calculations confirm that increasing the H coverage on a NP representative of S1 causes a sizable expansion of the first NN median-bond length. Namely, $R(\text{Pt}_{22}) < R(\text{Pt}_{22}\text{H}_{22}) < R(\text{Pt}_{22}\text{H}_{25}) < R(\text{Pt}_{22}\text{H}_{27}) < R(\text{Pt}_{22}\text{H}_{29}) < R(\text{Pt}_{22}\text{H}_{31})$. In order to establish a comparison with the experiments, we turn to the H-adsorption Gibbs phase diagram, which allows us to determine the thermodynamically stable H coverage at the temperature of interest. It should be noted that for Pt₂₂ (S1) a wider bond-length distribution is observed in the presence of H, and that the median value is reported in Fig. 3(b). In general, longer Pt-Pt bonds were obtained when H was incorporated into the model for unsupported NP samples (see Table II). With increasing hydrogen coverage, the calculated contractions for Pt₂₂H_M (0 K) with respect to bulk Pt were found to decrease from 4% to 2.1%. However, these values are significantly larger than the maximum contraction observed experimentally (0.4–0.6% at ~ 170 K).

The intrinsic thermally driven bond-length expansion of a support-free Pt₂₂ NP was calculated via *ab initio* MD [Fig. 3(b) (open symbols)]. The theoretical thermal-expansion coefficient α was found to be positive ($\sim +28 \times 10^{-6} \text{ K}^{-1}$) and larger than that of bulk Pt. Figure 3(b) also displays similar data obtained for H-covered NPs (closed symbols). The latter data were based on the Gibbs phase diagram [see Eq. (1)] calculated for Pt₂₂H_M, which is displayed in Fig. 3(c). From the H coverages studied, the thermodynamically stable configurations are those with all H atoms around edge Pt atoms, namely, Pt₂₂H₂₉ below 400 K, Pt₂₂H₂₅ at ~ 500 K, and Pt₂₂H₂₂ above 600 K. Our calculations for the H coverages selected suggest that, at a constant H₂ pressure of 1 atm, H desorption sets in at about 420 K, marked by a vertical dotted line in Fig. 3(c). The latter is the temperature for which an intercept of the G^{GAIN} adsorption curves corresponding to Pt₂₂H₂₉ and Pt₂₂H₂₅ is observed, indicating the higher stability of NP configurations partially depleted of hydrogen at edge sites and

totally depleted of H at the facets. It may also be considered as an upper limit for the H-desorption onset temperature, since intermediate states (Pt₂₂H₃₀, Pt₂₂H₂₈, and Pt₂₂H₂₆) were not considered. Since the Pt-Pt bond lengths vary as a function of H coverage (see Table II), the evolution of the bond-length with increasing temperature (and decreasing H coverage) can be estimated. Following these considerations, a thermal expansion coefficient of $\sim -47 \times 10^{-6} \text{ K}^{-1}$ was obtained. This coefficient reflects the thermally induced desorption of H under conditions which mimic the experimental environment (with the exception of the lack of support). The large and negative thermal expansion coefficient obtained for the Pt₂₂H_M NP is in clear contrast with the positive value calculated for adsorbate-free Pt₂₂.

D. Vibrational properties

The eigenfrequencies and eigenvectors of unsupported, clean Pt NPs and H-covered NPs were calculated from first principles.⁵⁷ Both $\langle \sigma_d^2 \rangle_{\text{th}}$ and $\langle x^2 \rangle_{\text{th}}$ were obtained exactly within the harmonic approximation from the discrete spectrum of the NPs. Figure 5(a) contains information on the thermal evolution of $\langle \sigma_d^2 \rangle_{\text{th}}$ of Pt₂₂H₂₂, Pt₂₂H₂₅, Pt₂₂H₂₉, and (b) of clean Pt NPs (Pt₂₂, Pt₃₃, Pt₄₄, Pt₅₅, and Pt₈₅). The evolution of $\langle x^2 \rangle_{\text{th}}$ for the former adsorbate- and support-free Pt NPs is shown in (c). The thermal evolution of $\langle \sigma_d^2 \rangle_{\text{th}}$ of Pt₂₂H₂₂, Pt₂₂H₂₅, and Pt₂₂H₂₉ shows that $\langle \sigma_d^2 \rangle_{\text{th}}$ and its slope varies as H desorbs with increasing temperature. Furthermore, the slopes of $\langle \sigma_d^2 \rangle_{\text{th}}$ for all three H-covered NPs (Pt₂₂H₂₂, Pt₂₂H₂₅, and Pt₂₂H₂₉) are larger than that of bulk Pt (exp.) and Pt₂₂ (theory). By comparing Figs. 5(b) and 5(c) it is evident that the trends obtained for $\langle \sigma_d^2 \rangle_{\text{th}}$ corresponding to the correlated motion of atom pairs within the NPs parallel to the bond are clearly different from those of the “real” (uncorrelated) MSDs, $\langle x^2 \rangle_{\text{th}}$. More specifically, smaller slopes of the $\langle \sigma_d^2 \rangle_{\text{th}}$ versus temperature plots were observed for the majority of the clean NPs as compared to bulk Pt (exp.), which is in qualitative agreement with

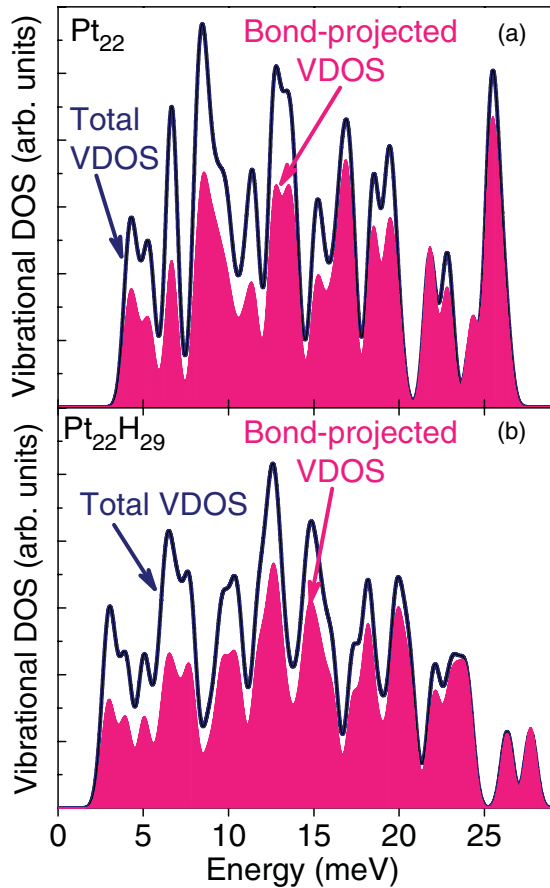


FIG. 7. (Color online) DFT-calculated total (black curve) and average bond-projected (pink/gray) VDOS of unsupported (a) Pt_{22} and (b) $\text{Pt}_{22}\text{H}_{29}$ NPs. Both are broadened by a Gaussian smearing of 0.35 meV. The pink/gray curve is representative of the lattice vibrations probed by EXAFS, which is expected to underestimate low-energy phonon modes.⁵⁷

the experimental data in Fig. 5(a). However, the contrary is true for the $\langle x^2 \rangle_{\text{th}}$ [Fig. 5(c)], with larger atomic displacements and slopes for the NPs as compared to bulk Pt. For all NPs, $\langle \sigma_d^2 \rangle_{\text{th}}$ and its slope are significantly smaller than $\langle x^2 \rangle_{\text{th}}$ and its slope.

It should be noted that clear differences exist between the calculated $\langle x^2 \rangle_{\text{th}}$ and $\langle \sigma_d^2 \rangle_{\text{th}}$ since the latter only takes into account the projection of the vibrational displacement along the bond (fluctuations parallel to the bond), in accordance with the theory of EXAFS.⁵⁹ Hence, it can be assumed that only the part of the vibrational density of states (VDOS) that is along the interatomic bond is representative of the lattice vibrations probed by EXAFS. Figure 7 illustrates the difference between the calculated total and bond-projected VDOS of Pt_{22} (a) and $\text{Pt}_{22}\text{H}_{29}$ (b) with the highest distinction (i.e., lower bond-projected VDOS) being observed at low energy. Therefore, by comparing the two types of VDOS curves in Fig. 7, the overall reduction of the bond-projected VDOS as compared to the total VDOS (averaged over all possible pairs of atoms in a NP) is considered responsible for the smaller values of $\langle \sigma_d^2 \rangle_{\text{th}}$ with respect to $\langle x^2 \rangle_{\text{th}}$ [Figs. 5(b) and 5(c)]. Furthermore, as shown in Fig. 5(c), $\langle x^2 \rangle_{\text{th}}$ of our

clean and unsupported NPs depends on the size and shape of the NPs.²⁸

Figure 6(a) displays Θ^{slope} , a parameter defined in correspondence with the Debye temperature (see definition for bulk materials in the experimental section⁴⁷) extracted from the slope of the theoretical $\langle \sigma_d^2 \rangle_{\text{th}}$ versus T plots of clean Pt_{22} (S1) and $\text{Pt}_{22}\text{H}_{22}$ [see Eq. (2)]. The $\text{Pt}_{22}\text{H}_{22}$ coverage was selected because it is stable at the highest temperature investigated ($T > 600$ K). The error bar corresponds to the variations of Θ^{slope} with H coverage, considering only those that are thermodynamically stable. Overall, the adsorption of hydrogen was found to lead to a reduction of Θ^{slope} for all H coverages studied. Nevertheless, the observed changes were nonmonotonic, being largest for $\text{Pt}_{22}\text{H}_{29}$ ($\Theta^{\text{slope}} = 226$ K) and smallest for $\text{Pt}_{22}\text{H}_{25}$ ($\Theta^{\text{slope}} = 203$ K), with $\text{Pt}_{22}\text{H}_{22}$ ($\Theta^{\text{slope}} = 220$ K) in between [Fig. 6(a)].

IV. DISCUSSION

Our calculations show that clean and unsupported NPs display an overall bond length contraction (averaged over all bonds within a NP) of about 6% at 0 K for Pt_{22} with respect to bulk Pt, whereas for the smallest experimental NPs measured in H_2 (S1), the contraction measured at 172–188 K is only 0.4% (Table II). This cannot be assigned to the difference in the experimental and theoretical temperatures [see Fig. 3(a)] but rather to the presence of H_2 (dissociate adsorption) on the experimental Pt NPs. Indeed, a better agreement is obtained when H is incorporated into the model of the unsupported NP. Our calculations corroborate that H partially lifts the Pt-Pt bond-length contraction caused by the low-coordination of surface atoms of the small NPs. More specifically, while for clean Pt_{22} the calculated R is contracted by $\sim 5.9\%$ with respect to the calculated value for bulk Pt (see Table II), for $\text{Pt}_{22}\text{H}_{29}$ (stable configuration below ~ 420 K), $\text{Pt}_{22}\text{H}_{25}$ (stable between ~ 420 and ~ 550 K), and $\text{Pt}_{22}\text{H}_{22}$ (stable above ~ 550 K), contractions of only ~ 2.3 , 3.1 , and 4.0% , respectively, were obtained. However, it should be mentioned that our calculations for the flat Pt_{22} NP did not result in the enhanced structural ordering expected for such NPs in the presence of H.³⁹

All of our NP samples were found to have smaller thermal expansion coefficients than bulk Pt [$\alpha \sim 11 \times 10^{-6} \text{ K}^{-1}$ is the reference value extracted from EXAFS measurements on a Pt foil or $8.8 \times 10^{-6} \text{ K}^{-1}$ from Ref. 61]. This effect can be partially assigned to the influence of the NP/support interface, since $\gamma\text{-Al}_2\text{O}_3$ is characterized by a smaller α of $\sim 4.5 \times 10^{-6} \text{ K}^{-1}$.⁶² The latter has also been held responsible for the reduced coefficient of thermal expansion measured for superheated Al NPs in Al_2O_3 .⁶³ Furthermore, for identically synthesized NPs, Fig. 4 constitutes a clear example of the influence of the NP size and geometry on their thermal properties. For reference, model shapes for our small NPs extracted from the analysis of EXAFS and TEM data are included in Table I and as insets in Fig. 6(b). Interestingly, Fig. 4(b) reveals a cross-over from positive to negative thermal expansion at/below 1 nm. This result is in agreement with data from Kang *et al.*⁵ and Sanchez *et al.*⁶ obtained for 0.9–1.1 nm Pt NPs supported on $\gamma\text{-Al}_2\text{O}_3$ prepared by impregnation precipitation. According to previous DFT calculations for Pt_{13} on dehydrated

γ -Al₂O₃ (with relatively strong metal/support interactions),⁶³ the impregnation-precipitation preparation method is likely to result in 2D-shaped NPs. In our study, the three samples displaying negative thermal expansion coefficients include the smallest NPs (S1 and S2, ~ 0.8 nm with 2D and 3D shape, respectively) and a sample with slightly larger NP size but 2D shape (~ 1 nm, S4). Since other samples with average NP size of ~ 1 nm but 3D shape did not show such effect (S3, S5, S6), both the NP/support interface and the ratio Pt surface atoms with adsorbed H (N_s sites) must be key parameters responsible for the anomalous thermodynamic behavior observed. In fact, the largest negative thermal expansion coefficient obtained for our micellar Pt NPs in H₂ was $-10 \times 10^{-6} \text{ K}^{-1}$ for the 2D NPs in S1, which is comparable with that reported by Kang *et al.*⁵ for 0.9 nm Pt NPs ($-13 \times 10^{-6} \text{ K}^{-1}$), on γ -Al₂O₃ also measured in H₂. Interestingly, larger negative α values were measured for the 3D NPs in S2 on γ -Al₂O₃ under He ($-15 \times 10^{-6} \text{ K}^{-1}$, not shown in Fig. 4) as compared to H₂ ($-3 \times 10^{-6} \text{ K}^{-1}$). The latter is assigned to the stronger Pt-Pt contraction (He data) since hydrogen relaxes the experimental Pt-Pt distances.²⁸

Our results demonstrate that adsorbates on the surface of small NPs influence their thermal expansion significantly. Our *ab initio* MD calculations show that the large negative α is not *intrinsic* to the NPs, since for support- and adsorbate-free Pt NPs (e.g., Pt₂₂), a large positive thermal expansion coefficient was obtained ($\sim +28 \times 10^{-6} \text{ K}^{-1}$). Our DFT calculations revealed that the bond-length contraction observed experimentally for small Pt NPs with increasing measurement temperature was partially extrinsic, and due to the contribution of H-desorption, Fig. 3(b). The Gibbs phase diagram in Fig. 3(c) gives a strong indication of the higher stability of NP configurations partially depleted of H, even when considering a constant pressure of 1 atm of pure H₂ around the NPs (50% H₂ and 50% He in the experimental case). More specifically, with increasing temperature Pt₂₂H_M configurations with decreasing M from 29 to 22 were found to be more thermodynamically stable. The temperature at which an intercept between the $M = 29$ and $M = 25$ curves is observed [marked by a vertical dotted line in Fig. 3(c)] can be used to estimate an upper limit for the activation energy for H desorption. Moreover, it should be noted that because of the dependence of G^{GAIN} on the chemical potential [see Eq. (1)], the onset of H desorption might happen at a lower temperature for smaller concentrations of H₂. Although we did not sample all the possibilities regarding H coverages and geometry, our calculations demonstrate that small amounts of H desorbing from the NPs are sufficient to decrease dramatically the median value of the Pt-Pt bond length in Pt₂₂ [Fig. 3(b)]. More specifically, even without taking into account the stiff substrate, the temperature-dependent desorption of H already resulted in a calculated *negative* thermal expansion coefficient about five times larger [$\sim -47 \times 10^{-6} \text{ K}^{-1}$ extracted from Fig. 3(b) closed symbols] than that measured via EXAFS for the supported NPs in S1 ($\sim -10 \times 10^{-6} \text{ K}^{-1}$) [Fig. 4(a)]. The contribution related to the desorption of H is necessarily compensated by the *intrinsic* thermally driven expansion of the Pt-Pt bonds observed for the unsupported, clean model NPs [Fig. 3(b), open symbols]. With both contributions at hand, one could see that the two effects combined can account qualitatively for the observed negative α , at least

once the onset temperature for H desorption has been reached [see Fig. 3(c)].

In addition to adsorbate effects and size-dependent changes in the geometry (and therefore, electronic properties) of small NPs, NP/support interactions also appear to be of significance for the understanding of their thermal properties. Previous calculations by Vila *et al.*⁷ on H-free Pt₁₀ clusters deposited on dehydrated γ -Al₂O₃ revealed a small but negative thermal-expansion trend attributed to changes in the bond lengths as the NP diffuses on the substrate, which is in clear contrast with our results for the larger, adsorbate-free, but unsupported Pt₂₂ clusters. The latter emphasizes the important role of the substrate. At the same time, these calculations reported significantly smaller Pt-Pt contractions ($\sim 3\%$ smaller) than those measured experimentally by the same group,⁷ which we assign to the adsorbate effect described previously. Our experimental data also provide evidence for the important role of the γ -Al₂O₃ substrate. For example, sample S4, with similar surface/volume ratio and NP/support contact area as S1 ($N_s/N_t = 0.82$ – 0.86 and $N_c/N_t = 0.55$ for these two samples) but larger average size (~ 1 nm for S4 and ~ 0.8 nm for S1), showed a lower but still negative thermal-expansion coefficient. When samples containing small NPs with the same size and analogous surface area for H₂-chemisorption are compared (e.g., S1 and S2, ~ 0.8 nm; $N_s/N_t = 0.84$ – 0.86 , Table I), the negative thermal-expansion effect was found to be more pronounced for sample S1 with the highest NP/support contact area ($N_s/N_t = 0.55$ for S1 versus $N_s/N_t = 0.23$ for S2). The specific role of the NP support is yet to be determined, since our present calculations were carried out on unsupported NPs, and only one support (γ -Al₂O₃) was used for all experiments. Nevertheless, a recent EXAFS study by Sanchez *et al.*⁶ revealed clear changes in the thermal-expansion behavior of Pt NPs prepared by the deposition-impregnation method and supported on γ -Al₂O₃ and C substrates, with positive α values reported for the clusters deposited on the more weakly interacting C support and negative α on γ -Al₂O₃.

In addition to the intriguing thermal-expansion behavior of our fcc Pt NPs supported on γ -Al₂O₃, Fig. 5(a) reveals clear differences in their thermodynamic properties with respect to bulk Pt, with smaller (σ_d^2) versus temperature slopes for the H-coated experimental NP samples. This result can be partially explained by the fact that EXAFS measurements underestimate the relative contribution of low-energy vibrational modes to the total σ_d^2 , an effect that we have theoretically demonstrated to be significant for small unsupported NPs. This can be seen in Fig. 7, where the calculated VDOS of Pt₂₂ and Pt₂₂H₂₉ is displayed together with the bond-projected VDOS (weighted similarly to the EXAFS data by only considering bond-length fluctuations parallel to the bond). From the comparison of the total and bond-projected VDOS in Fig. 7, it is confirmed that the main differences are observed at low energies, and that this region of the VDOS largely involves fluctuations perpendicular to the bond. Therefore, the experimental dynamic bond-projected bond length fluctuations can only be compared directly to $(\sigma_d^2)_{\text{th}}$ since the real MSD $\langle x^2 \rangle_{\text{th}}$ lacks the former EXAFS-weighting factor. Nevertheless, for the small (< 1.5 nm) unsupported NPs, we have confirmed numerically that $\langle x^2 \rangle_{\text{th}}$ depends on the size and shape of the NPs, as shown in Fig. 5(c) and described in more detail

in Ref. 57. Our calculations also demonstrate that $\langle x^2 \rangle_{\text{th}}$, and thereby $(\sigma_d^2)_{\text{th}}$, correlate with the behavior of the VDOS at low energy (Fig. 7). Small $\langle x^2 \rangle_{\text{th}}$ versus T slopes [and $(\sigma_d^2)_{\text{th}}$ versus T slopes] were observed for NPs with a large phonon-confinement gap at low energies.⁵⁷ Such a vibrational confinement gap⁶⁴ is in turn determined by the NP size and shape.⁵⁷ For example, Pt₄₄ (S2) has the smallest $\langle x^2 \rangle_{\text{th}}$ and the widest phonon gap (5.7 meV), and Pt₃₃ (S4) has the largest $\langle x^2 \rangle_{\text{th}}$ and smallest gap (~ 2.5 meV).⁵⁷ This apparently small difference in the VDOS is critical, as seen by the visible deviation of the $\langle x^2 \rangle_{\text{th}}$ and $(\sigma_d^2)_{\text{th}}$ of Pt₃₃ with respect to the rest of the samples in Figs. 5(b) and 5(c). Additionally, within the set of samples analyzed, an increase in the NP size for the same NP shape (S2 with 44 atoms versus S3 with 85 Pt atoms) was found to increase $\langle x^2 \rangle_{\text{th}}$ [Fig. 5(c)].

It is useful to point out that since a number of low-energy vibrational modes correspond to shear perturbations of surface atoms,^{65,66} if the NPs are strongly bound to a stiff substrate, the corresponding boundary condition might eliminate some of those modes.^{57,67} In addition, the presence of a strongly binding support might lead to an increase in the phonon gap present for small NPs.⁵⁴ For instance, the vibrational gap increased from 0.2 to 4.2 meV for free versus pseudomorphic Ru(0001)-supported single-layer Au₁₃.^{57,68} Therefore, for NPs supported on stiff substrates in which the low-energy VDOS might be suppressed, the differences between $\langle x^2 \rangle$ and σ_d^2 measured via EXAFS might not be as significant as those shown in Fig. 5 for the unsupported theoretical NPs. Thus, quantitative agreement between theoretical and experimental data requires also the consideration of the support in the calculations, which for the various NP sizes and shapes investigated here is beyond our possibilities based on first principle calculations. Moreover, it should be noted that the calculations shown in Fig. 5(a) of σ_d^2 versus T curves for Pt₂₂H₂₂, Pt₂₂H₂₅, and Pt₂₂H₂₉ intend to single out the effect of the limited sensitivity of EXAFS to low E-vibrational modes but do not take into consideration the expected changes upon gradual desorption of H₂ with increasing temperatures, since they correspond to a constant hydrogen coverage.

From the slope of the σ_d^2 versus T plot of the EXAFS data in Fig. 5(a), a Debye temperature was obtained for NPs in the size range of 0.8 to 5.4 nm (Fig. 6). As we have already mentioned, the behavior of the Debye temperature signifies here only the trends in the MSBLFs. It neither validates nor refutes the Debye model for the VDOS, which has been noted to be unsuitable for accurately describing the vibrational properties of small unsupported NPs (<500 atoms,⁶⁴ <2 nm) due to the 3N-discretization of the vibrational energies^{66,69} and the observation of an excess VDOS at low phonon energies.⁷⁰ The following observations are made based on the analysis of the EXAFS data shown in Fig. 6: (i) an overall increase in the Debye temperature of all NP samples with respect to bulk Pt; (ii) the distinct thermal properties of small and large Pt NPs. For NPs ≤ 1 nm, a decrease in Θ_D is observed with decreasing NP size, while for larger NPs (>1 nm), the Debye temperature was found to decrease with increasing NP diameter [Fig. 6(a)]. The Θ_D value of bulk Pt was not reached for the largest NPs investigated here (~ 5.4 nm). The size dependency displayed by the NPs with sizes >1.5 nm is in agreement with that reported for superheated NPs with well-ordered (epitaxial)

NP/support interfaces.³ (iii) For NPs <1.5 nm, a decrease in Θ_D is also obtained with increasing relative number of atoms at the NP surface (N_s) [Fig. 6(b)]. It should be taken into consideration that N_s here includes surface and perimeter atoms (the latter in contact with the support). A plausible explanation for this observation is the consideration of the low-coordinated surface atoms as defects leading to a suppression of Θ_D , while the perimeter atoms in contact with the support might have the contrary effect. In fact if the interaction of Pt atoms with γ -Al₂O₃ is responsible for the large experimental Θ_D , increasingly large 3D NPs will have a smaller fraction of atoms in contact with the support, which would lead to the disappearance of the Θ_D -enhancement (bulk limit). This trend is observed here for the largest NPs investigated (S9).

Although we did not measure the melting temperature of our NPs directly, according to Eq. (3), similar size-dependent trends are expected for T_m and Θ_D .²⁷

$$T_m = \frac{2\pi m c^2 R^2 \Theta_D^2 k_B}{h^2}, \quad (3)$$

with m being the atomic mass, c Lindemann's constant,²⁶ R the bond length, k_B Boltzmann constant, and h the Planck constant.

In the literature³ the following factors have been discussed to contribute to the Θ_D (or T_m) enhancement reported for some nanoscale systems: (i) the presence of a matrix (e.g., γ -Al₂O₃) with a higher melting temperature than that of the NPs (e.g., Pt) or a high melting-temperature coating around the NPs, and/or a support that binds strongly the NPs; (ii) a low density of structural defects within the NPs, good crystallinity, and NP faceting; (iii) a NP/support interface with a low-defect density and, if possible, an epitaxial relation between the NP/support; and (iv) the absence of a significant number of grain boundaries, twinning, and other related structural defects. The sample preparation method is a key factor controlling the structural features affecting this anomalous thermodynamic behavior. Our large NPs (>1.5 nm) display a trend for the Debye temperature analogous to that reported for the melting temperature of melt-spun *superheated* in NPs embedded in Al³³ or Pb NPs in Al,⁷¹ namely, increasing Θ_D with decreasing NP size. Interestingly, for the same experimental systems, differently prepared samples (ball-milled) with incoherent NP/matrix interfaces displayed the opposite trend, namely, decreasing T_m with decreasing NP size.^{33,71} These effects were explained in terms of an enhanced internal disorder and noncoherent NP/support interface for the latter set of samples. Cahn³⁴ attributes superheating effects to a constraint in the amplitude of the vibration of atoms at the NP/support interface, highlighting the importance of an epitaxial relation between the metal NPs and the coating, matrix, or support material. In our case Fig. 5(a) might suggest an overall stiffening of our NPs because of the reduced bond-projected bond length fluctuations, although the data shown correspond to the entire NP, not only to atoms at the NP/support interface. Nevertheless, as is shown in Fig. 5(b), a large part of the reduction in σ_d^2 of the experimental NPs as compared to bulk Pt (and therefore part of the reduction of the slopes giving rise to enhanced Θ_D) can be assigned to the

distinct definition of the EXAFS σ_d^2 (correlated bond-projected bond-length fluctuations), as compared to the real mean-square vibrational amplitude $\langle x^2 \rangle_{\text{th}}$ [Fig. 5(c)]. On the other hand it should be kept in mind that our calculations suggest that H reduces the slope of $(\sigma_d^2)_{\text{th}}$, but they do not include the γ -Al₂O₃ substrate, which is expected to increase it and thus play a pivotal role in the thermodynamic behavior of supported NPs.

Following the preceding ideas, the enhanced Debye temperatures observed for our large NPs ($1.5 \text{ nm} < d < 5 \text{ nm}$) and their size dependency appear typical of well-ordered, faceted NPs with coherent or semicoherent NP/support interfaces surrounded by a high melting-temperature matrix (or support in our case). The crystallinity of our large NPs can be seen in the EXAFS spectra included in Fig. 2(a) (4–6 Å range) (S8) as compared to a bulk Pt reference. On the other hand our small NPs (S1–S6 $\leq 1 \text{ nm}$) behave similarly to disordered NPs, for which a decreasing melting temperature was observed with decreasing NP size.³³ Furthermore, when small NPs are considered, not just the NP size but also their shape might strongly affect their Debye temperatures. For example, we obtained different Debye temperatures for NPs of identical size ($\sim 1 \text{ nm}$ TEM diameter, S3–S6), and a correlation was observed between the number of low coordinated atoms at the NP surface and Θ_D , with lower Θ_D values for the NPs with the highest surface-to-volume ratio [Fig. 6(b)]. This trend can also be explained by the adsorbate effect since the higher the surface-to-volume ratio, the stronger the adsorbate effect will be. Our theoretical results on unsupported Pt₂₂H_M revealed that the adsorption of hydrogen increases the MSBLFs and its slope [$(\sigma_d^2)_{\text{th}}$ versus T] with respect to the corresponding values of adsorbate-free Pt₂₂, leading to a smaller Θ_D [Fig. 6(a)]. Nevertheless, it should be noted that the support, which is expected to have the opposite effect, still needs to be taken into account. Experimentally, it was observed that the flat NPs in S4 displayed a higher Θ_D than analogously sized 3D clusters (S3) with a lower contact area with the γ -Al₂O₃ substrate. This effect reveals the important role played by the NP/support interface in the thermodynamic properties of small NPs.

Summarizing, our experimental and theoretical data provide insight into the influence of the geometric structure (size and shape) and environment (adsorbates and substrate) in the thermodynamic properties of metal NPs. In particular the important role of H₂ desorption in the negative thermal expansion experimentally observed for small supported metal clusters is discussed. Furthermore, size-dependent changes in the Debye temperature observed via EXAFS are explained in terms of the NPs geometrical structure and NP/support interface but also as a function of intrinsic limitations of the experimental technique used.

V. CONCLUSIONS

A synergistic combination of EXAFS, TEM, NP-shape modeling, *ab initio* total energy, and MD calculations based

on DFT have allowed us to gain insight into the structure and thermal properties of Pt NPs supported on γ -Al₂O₃. Our main experimental findings are (i) a size-dependent cross-over from positive to negative thermal expansion with decreasing NP size; (ii) the observation of enhanced experimental Debye temperatures for small Pt NPs bound to γ -Al₂O₃; (iii) the different vibrational behavior of large and small metal NPs. Small NPs ($\leq 1.5 \text{ nm}$) show a general decrease in the Debye temperature with decreasing NP size associated with the increase in the number of atoms at the NP surface. For large NPs ($> 1.5 \text{ nm}$), decreasing Debye temperatures are observed with increasing NP size. For the latter samples the existence of a decreasing number of atoms within the NPs in contact with the support appears to contribute to the suppression of the matrix-induced Θ_D -enhancement.

Our computational investigations revealed that the negative thermal expansion of the smallest NPs is not intrinsic and qualitatively suggest that thermal desorption of chemisorbed hydrogen is at least partially responsible for this effect. The comparison of the calculated bond-projected $(\sigma_d^2)_{\text{th}}$ (based on the CDM) and the total $\langle x^2 \rangle_{\text{th}}$ for unsupported and adsorbate-free NPs revealed smaller slopes in the $(\sigma_d^2)_{\text{th}}$ versus T plots. Hence, the relatively small experimental σ_d^2 slopes, and therefore, the unusually large Debye temperatures obtained experimentally, can be partially assigned to the nature of the experimental probe used for its determination, since fluctuations in the bond length perpendicular to the bond, which might be present at low energies, are not accessible to EXAFS. Furthermore, our calculations traced the observed decrease in the MSDs or bond-length fluctuations to the possible elimination of low-energy vibrational modes of the NPs. We have shown that this might occur due to specific detection limits of the experimental technique used, by the presence of large gaps in the VDOS of the NPs, or due to NP/support interactions.

ACKNOWLEDGMENTS

The authors are grateful to Anatoly Frenkel (Yeshiva Univ.) for assistance with the EXAFS measurements and data analysis and to N. Marinkovic and Q. Wang (BNL) for beamline support. M.A.O. is indebted to Sergey Stolbov for enlightening discussions. The EXAFS and NP shape-modeling work was made possible thanks to funding from the US National Science Foundation (DMR-0906562). The theoretical work was supported by the Office of Basic Energy Sciences of the US Department of Energy (DE-FG02-07ER46354) and the microscopy studies by DE-FG02-03ER15476. Synchrotron Catalysis Consortium facilities at NSLS where the EXAFS measurements were conducted are also funded by DOE (DE-FG02-05ER15688). NSLS is supported by the US Department of Energy (DE-AC02-98CH10866). NCFP at University of Pittsburgh is acknowledged for the use of JEM 2100F.

*Corresponding author: roldan@ucf.edu

†Corresponding author: Marisol.AlcantaraOrtigoza@ucf.edu

¹M. Valden, X. Lai, and D. W. Goodman, *Science* **281**, 1647 (1998).

²A. Naitabdi and B. Roldan Cuenya, *Appl. Phys. Lett.* **89**, 043101 (2006).

³Q. S. Mei and K. Lu, *Prog. Mater. Sci.* **52**, 1175 (2007).

- ⁴G. D. Barrera, J. A. O. Bruno, T. H. K. Barron, and N. L. Allen, *J. Phys. Condens. Matter* **17**, R217 (2005).
- ⁵J. H. Kang, L. D. Menard, R. G. Nuzzo, and A. I. Frenkel, *J. Am. Chem. Soc. Comm.* **128**, 12068 (2006).
- ⁶S. I. Sanchez, L. D. Menard, A. Bram, J. H. Kang, M. W. Small, R. G. Nuzzo, and A. I. Frenkel, *J. Am. Chem. Soc.* **131**, 7040 (2009).
- ⁷F. D. Vila, J. J. Rehr, J. Kas, R. G. Nuzzo, and A. I. Frenkel, *Phys. Rev. B* **78**, 121404 (2008).
- ⁸V. Juve, A. Crut, P. Maioli, M. Pellarin, M. Broyer, N. del Fatti, and F. Vallee, *Nano Lett.* **10**, 1853 (2010).
- ⁹M. Schmidt, R. Kusche, B. von Issendorff, and H. Haberland, *Nature* **393**, 238 (1998).
- ¹⁰Z. Y. Lu, C. Z. Wang, and K. M. Ho, *Phys. Rev. B* **61**, 2329 (2000).
- ¹¹P. Buffat and J.-P. Borel, *Phys. Rev. A* **13**, 2287 (1976).
- ¹²B. Gilbert, F. Huang, H. Zhang, G. A. Waychunas, and J. F. Banfield, *Science Express* **305**, 651 (2004).
- ¹³J. Rockenberger, L. Troger, A. Kornowski, T. Vossmeier, A. Eychmuller, J. Feldhaus, and H. Weller, *J. Phys. Chem. B* **101**, 2691 (1997).
- ¹⁴J. Rockenberger, L. Troger, A. L. Rogach, M. Tischer, M. Grundmann, A. Eychmuller, and H. Weller, *J. Chem. Phys.* **108**, 7807 (1998).
- ¹⁵L. J. Giovanetti, J. M. Ramallo-Lopez, F. G. Requejo, D. I. Garcia-Gutierrez, M. J. Yakaman, and A. F. Craievich, *J. Phys. Chem. C* **111**, 7599 (2007).
- ¹⁶L. L. Araujo, P. Kluth, G. M. Azevedo, and M. C. Ridway, *Phys. Rev. B* **74**, 184102 (2006).
- ¹⁷M. Dubiel, J. Haug, H. Kruth, H. Hofmeister, and W. Seifert, *J. Phys.: Conf. Series* **190**, 012123 (2009).
- ¹⁸P. Z. Pawlow, *Phys. Chem.* **65**, 545 (1909).
- ¹⁹G. L. Allen, R. A. Bayles, W. W. Giles, and W. A. Jesser, *Thin Solid Films* **144**, 297 (1986).
- ²⁰T. Comaschi, A. Balerna, and S. Mobilio, *Phys. Rev. B* **77**, 075432 (2008).
- ²¹T. Yokoyama, S. Kimoto, and T. Ohta, *Jpn. J. Appl. Phys.* **28**, 851 (1989).
- ²²M. Dippel, A. Maier, V. Gimple, H. Wider, W. E. Evenson, R. L. Rasera, and G. Schatz, *Phys. Rev. Lett.* **87**, 095505 (2001).
- ²³S. L. Lai, J. Y. Guo, V. Petrova, G. Ramanath, and L. H. Allen, *Phys. Rev. Lett.* **77**, 99 (1996).
- ²⁴B. H. Morrow and A. Striolo, *Nanotechnology* **19**, 195711 (2008).
- ²⁵Y. H. Wen, H. Fang, Z. Z. Zhu, and S. G. Sun, *Phys. Lett. A* **373**, 272 (2009).
- ²⁶F. A. Lindemann, *Physik Z.* **11**, 609 (1910).
- ²⁷H.-J. Hoffmann, *Materialwissenschaft und Werkstofftechnik* **35**, 79 (2004).
- ²⁸B. Roldan Cuenya, A. I. Frenkel, S. Mostafa, F. Behafarid, J. R. Croy, L. K. Ono, and Q. Wang, *Phys. Rev. B* **82**, 155450 (2010).
- ²⁹R. Giulian, L. L. Araujo, P. Kluth, D. J. Sprouster, C. S. Schnorr, G. J. Foran, and M. C. Ridway, *J. Phys. Condens. Matter* **21**, 155302 (2009).
- ³⁰Q. Xu, I. D. Sharp, C. W. Yuan, D. O. Yi, C. Y. Liao, A. M. Glaeser, A. M. Minor, J. W. Beeman, M. C. Ridgway, P. Kluth, J. W. Ager, III, D. C. Chrzan, and E. E. Haller, *Phys. Rev. Lett.* **97**, 155701 (2006).
- ³¹S. W. Marshall and R. M. Wilenzick, *Phys. Rev. Lett.* **16**, 219 (1966).
- ³²Q. F. Gu, G. Krauss, W. Seurer, F. Gramm, and A. Cervellino, *Phys. Rev. Lett.* **100**, 045502 (2008).
- ³³K. Lu and Z. H. Jin, *Curr. Opin. Solid State Mater. Sci.* **5**, 39 (2001).
- ³⁴R. W. Cahn, *Nature* **323**, 668 (1986).
- ³⁵W.-H. Li, S. Y. Wu, C. C. Yang, S. K. Lai, K. C. Lee, H. L. Huang, and H. D. Yang, *Phys. Rev. Lett.* **89**, 135504 (2002).
- ³⁶A. L. Ankudinov, J. J. Rehr, J. J. Low, and S. R. Bare, *Phys. Rev. Lett.* **86**, 1642 (2001).
- ³⁷M. K. Oudenhuijzen, J. H. Bitter, and D. C. Koningsberger, *J. Phys. Chem. B* **105**, 4616 (2001).
- ³⁸B. Roldan Cuenya, J. R. Croy, S. Mostafa, F. Behafarid, L. Li, Z. Zhang, J. C. Yang, Q. Wang, and A. I. Frenkel, *J. Am. Chem. Soc.* **132**, 8747 (2010).
- ³⁹S. N. Reifsnnyder, M. M. Otten, D. E. Sayers, and H. H. Lamb, *J. Phys. Chem. B* **101**, 4972 (1997).
- ⁴⁰S. C. Badescu, K. Jacobi, Y. Wang, K. Bedurftig, G. Ertl, P. Salo, T. Ala-Nissila, and S. C. Ying, *Phys. Rev. B* **68**, 205401 (2003).
- ⁴¹J. R. Croy, S. Mostafa, H. Heinrich, and B. Roldan Cuenya, *Catal. Lett.* **131**, 21 (2009).
- ⁴²A. Naitabdi, F. Behafarid, and B. Roldan Cuenya, *Appl. Phys. Lett.* **94**, 083102 (2009).
- ⁴³S. Mostafa, F. Behafarid, J. R. Croy, L. K. Ono, L. Li, J. C. Yang, A. I. Frenkel, and B. Roldan Cuenya, *J. Am. Chem. Soc.* **132**, 15714 (2010).
- ⁴⁴L. K. Ono, B. Yuan, H. Heinrich, and B. Roldan Cuenya, *J. Phys. Chem. C* **114**, 22119 (2010).
- ⁴⁵M. Newville, *J. Synchrotron Radiat.* **8**, 322 (2001).
- ⁴⁶E. Sevillano, H. Meuth, and J. J. Rehr, *Phys. Rev. B* **20**, 4908 (1979).
- ⁴⁷P. P. Lottici, *Phys. Rev. B* **35**, 1236 (1987).
- ⁴⁸A. I. Frenkel and J. J. Rehr, *Phys. Rev. B* **48**, 585 (1993).
- ⁴⁹A. L. Ankudinov, J. J. Rehr, J. J. Low, and S. R. Bare, *J. Chem. Phys.* **116**, 1911 (2002).
- ⁵⁰H. Kuroda, T. Yokoyama, K. Asakura, and Y. Iwasawa, *Faraday Discuss.* **92**, 189 (1991).
- ⁵¹See Supplemental Material at <http://link.aps.org/supplemental/10.1103/PhysRevB.84.245438> for additional experimental and computational details, including the determination of the NP shape from EXAFS data, fit-quality parameters, and third cumulant values from the analysis of the EXAFS data, temperature-dependent EXAFS data in k -space and r -space together with the corresponding fits and additional TEM images.
- ⁵²F. Behafarid and B. Roldan Cuenya, *Nano Lett.* (to be published) (2011) doi:10.1021/nl2027525.
- ⁵³P. Hohenberg and W. Kohn, *Phys. Rev.* **136**, B864 (1964).
- ⁵⁴G. Kresse and J. Furthmuller, *Phys. Rev. B* **54**, 11169 (1996).
- ⁵⁵G. Kresse and J. Joubert, *Phys. Rev. B* **59**, 1758 (1999).
- ⁵⁶J. P. Perdew, K. Burke, and M. Ernzerhof, *Phys. Rev. Lett.* **77**, 3865 (1996).
- ⁵⁷M. Alcántara Ortigoza, G. Shafai, and T. S. Rahman (unpublished).
- ⁵⁸M. Shiraiishi, T. Takenobu, and M. Ata, *Chem. Phys. Lett.* **367**, 633.
- ⁵⁹G. Beni and P. M. Platzman, *Phys. Rev. B* **14**, 1514 (1976).
- ⁶⁰Z. H. Jin and K. Lu, *Encyclopedia of Materials: Science and Technology* (Elsevier, Amsterdam, 2002).
- ⁶¹Y. S. Touloukian, *Thermophysical Properties of Matter* (Plenum Press, New York, 1975).
- ⁶²W. Y. Ching, L. Ouyang, P. Rulis, and H. Yao, *Phys. Rev. B* **78**, 014106 (2008).
- ⁶³Q. S. Mei, S. C. Wang, H. T. Cong, Z. H. Jin, and K. Lu, *Phys. Rev. B* **70**, 125421 (2004).

- ⁶⁴G. von Eynatten and H. E. Bömmel, *Appl. Phys.* **14**, 415 (1977).
- ⁶⁵R. Heid and K. P. Bohnen, *Phys. Rep.* **387**, 151 (2003).
- ⁶⁶M. Alcántara-Ortigoza, K. P. Bohnen, T. Rahman, R. Heid (unpublished).
- ⁶⁷B. Roldan Cuenya, A. Naitabdi, J. Croy, W. Sturhahn, J. Y. Zhao, E. E. Alp, R. Meyer, D. Sudfeld, E. Schuster, and W. Keune, *Phys. Rev. B* **76**, 195422 (2007).
- ⁶⁸G. Shafai, S. Hong, M. Bertino, and T. S. Rahman, *J. Phys. Chem. C* **113**, 12072 (2009).
- ⁶⁹G. A. Narvaez, J. Kim, and J. W. Wilkins, *Phys. Rev. B* **72**, 155411 (2005).
- ⁷⁰A. Kara and T. S. Rahman, *Phys. Rev. Lett.* **81**, 1453 (1998).
- ⁷¹H. Rossner and G. Wilde, *Scr. Mater.* **119**, 55 (2006).